

Probing the onset of hydrodynamization in peripheral p-Pb collisions at $\sqrt{s_{NN}} = 5.02$ TeV

Nikhil Hatwar,* Sadhana Dash, and Basanta Kumar Nandi
Indian Institute of Technology, Bombay, Powai, Mumbai, India
(Dated: March 19, 2025)

An attempt has been made to estimate the minimum size of the de-confined matter of Quark-Gluon Plasma (QGP) in small systems like p-Pb system that could be satisfactorily modeled with low-order hydrodynamics. The variation of second order transport coefficient of second order relativistic viscous hydrodynamics, the shear relaxation time has been utilized to study the sensitivity of experimental observables like elliptic flow coefficient. A representative system of p-Pb collisions at $\sqrt{s_{NN}} = 5.02$ TeV, simulated with the state-of-art framework of JETSCAPE event generator was used to study the variation of elliptic flow coefficient for peripheral collisions. The soft sector dynamics was simulated using an initial condition, a pre-equilibrium stage, hydrodynamics and a hadron afterburner. The transverse momentum spectra and rapidity distribution was obtained for light flavored hadrons and compared with the experimental data. The increase in elliptic flow fluctuations indicate breakdown of fluid behavior at $dN/dy \approx 14$ for p-Pb collision at $\sqrt{s_{NN}} = 5.02$ TeV.

I. INTRODUCTION

Over the last few decades, we have slowly gathered mounting indirect evidence of the production of a deconfined quark-gluon matter in relativistic heavy-ion collisions carried out at BNL's Relativistic Heavy Ion Collider and CERN's Large Hadron Collider [1, 2]. The focus is now shifting towards finding the properties of this phase of strongly interacting matter. However, the discovery of most of these Quark-Gluon Plasma (QGP) signatures in small systems like proton-nucleus and high multiplicity proton-proton collisions has been puzzling [3–6].

Currently we are confronted with the question of whether these signatures are a result of cold nuclear matter effects [7], genuine QGP-like hot nuclear matter effects [8], or is it something in-between [9]. Fig. 1 shows a cartoon of collision domains for varying nuclear mass (which represents the system size of collision) and collisional energy. In the domain of large collisional energy and large system size, we have convincing evidence of QGP formation, shown as a large red blob. At low collisional energy, we have nucleons and/or partons scattering off each other, represented by blue color. There is no consensus about the nature of medium produced for smaller system size and large collisional energy, represented by three red circles in Fig. 1. There should lie a threshold value of collisional energy for a suitably large collision system beyond which hot QCD matter could form [10, 11]. If there is no formation of a deconfined medium in small systems like proton-proton at large energies, there should lie another threshold of system size for which hot QCD matter could form. In the present study, we are trying to estimate this system size threshold marked as *system size deconfinement onset* in Fig. 1 for peripheral p-Pb collisions at $\sqrt{s_{NN}} = 5.02$ TeV.

Relativistic hydrodynamics has emerged as a key effective dynamics in modeling the QGP phase of high energy collisions [12]. The early phenomenological success of hydrodynamic description for collective expansions in the heavy-ion collisions indicated the formation of locally equilibrated isotropic matter as early as $1 \text{ fm}/c$ [13]. It was challenging to explain such a rapid transition from strong color field configuration to a locally thermalized system of quarks and gluons [14]. It was found that starting from various initial conditions, evolution of pressure anisotropy is accurately described by hydrodynamic gradient expansion. This surprising result indicated that the phenomenological success of hydrodynamics does not necessarily require early thermalization or even isotropization in the heavy-ion collisions [15]. Hence, a more appropriate question to ask would be: how far away from equilibrium, would hydrodynamics still be applicable [16, 17]? Prior studies have explored different ways to address this question using entropy density [18]. In Ref. [19], authors tried to quantify the applicability of hydrodynamics in terms of a dimensionless quantity termed as *opacity* which resolved the system sizes into three regimes viz. *particle-like*, *transition*, and *hydro-like*.

For a long time, hydrodynamics has been associated with thermodynamic equilibrium state. As the system under consideration is strictly not in local thermal equilibrium, the word "hydrodynamization" was coined by Casalderrey-Solana, Liu et al. [20] to distinguish the low-order viscous hydrodynamic constitutive relations from local thermalization. The usual approach to hydrodynamics involves expansion of the energy-momentum tensor in terms of gradients of fields. Here, the fundamental hydrodynamic fields are considered in the local rest frame to build the energy-momentum tensor ($T^{\mu\nu}$) of the system, satisfying the conservation equation ($\partial_\mu T^{\mu\nu} = 0$). With just the fields in energy-momentum tensor expression, we have the zeroth order of ideal hydrodynamics. If we include the first-order gradient which represents

* nikhil.hatwar@gmail.com

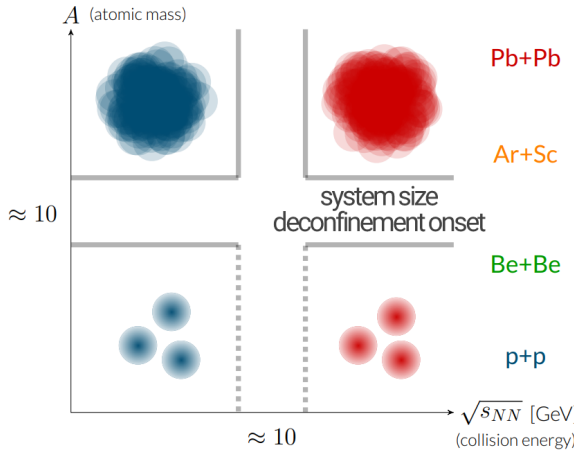


FIG. 1. Cartoon of collision domains for varying atomic mass and collisional energy. The three blue circles and the large blue blob at low collisional energy represent cold nuclear matter. The large red blob represents the QGP formation regime. The three small red circles represent a region where the nature of QCD matter produced is debatable. Figure adapted from Ref. [30].

the dissipative effects, we run into the causality violation problem of Navier Stokes equation[21]. Few studies have made progress in restoring causality at first order [22, 23]. With inclusion of second-order gradient, the formalisms differ on basis of the number or kind of terms kept in the constitutive relations, resulting in variations ,e.g., MIS [24–26], DNMR [27], aHydro [28], BRSSS [29].

There are signatures that the familiar hydrodynamic gradient expansion in general is not a convergent series [16]. To examine the collective modes of diverging gradient expansion, we usually consider the linear response of the energy-momentum tensor ($T^{\mu\nu}$) due to an arbitrary perturbing source, $S_{\gamma\delta}$ [31] as ,

$$\delta\langle T^{\mu\nu}\rangle(t, \mathbf{x}) = \int dt d^3x G^{\mu\nu,\gamma\delta}(t, \mathbf{x}) S_{\gamma\delta}, \quad (1)$$

where $G^{\mu\nu,\gamma\delta}(t, \mathbf{x})$ is the two-point retarded correlator, referred to as Green's function. The solution of this equation at late times is expressed as,

$$\delta\langle T^{\mu\nu}\rangle(t, \mathbf{x}) \sim e^{-i\omega_{\text{sing}}(k)t+i\mathbf{k}\cdot\mathbf{x}}, \quad (2)$$

where $\omega_{\text{sing}}(k)$ is the complex singularity of Fourier transformed two-point retarded correlator. The real part of this complex frequency is termed “hydrodynamic mode frequency” and is responsible for the excitation of equilibrium plasma. The imaginary part is referred to as “non-hydrodynamic mode frequency”, which causes dissipative effects. For BRSSS theory, these singularities have been worked out for sound channel [32] with the hydrodynamic mode frequency given as,

$$\omega_h^\pm = \pm \frac{k}{\sqrt{3}} - \frac{2i\eta k^2}{3Ts} + \dots \quad (3)$$

and the corresponding non-hydrodynamic mode frequency is given by,

$$\omega_{\text{nh}} = -i\left(\frac{1}{\tau_\pi} - \frac{4\eta k^2}{3sT}\right) + \dots \quad (4)$$

In the above equations (3) and (4), η is the shear viscosity, T is the temperature, s is the entropy density, k is the wave vector and τ_π is the second order transport coefficient called shear relaxation time. For vanishing wave vector these frequencies reduce to,

$$\lim_{k \rightarrow 0} \omega_h^\pm = 0 \quad ; \quad \lim_{k \rightarrow 0} \omega_{\text{nh}} = -\frac{i}{\tau_\pi} \quad (5)$$

The fact that ω_{nh} cannot be eliminated in the limit of $k \rightarrow 0$ is the defining feature of non-hydrodynamic mode.

The contemporary understanding of hydrodynamics indicates that the applicability of hydrodynamics is exclusively determined by the contribution of non-hydrodynamic mode relative to hydrodynamic mode. The fluid behavior will break down if the contribution of non-hydrodynamic mode exceeds that of hydrodynamic mode. The non-hydrodynamic mode is regulated by the second-order transport coefficient called shear relaxation time, as could be seen from Eq. (5).

The primary objective of this work is to study the behavior of elliptic flow for the extreme values of shear relaxation time for peripheral collisions in p-Pb collisions at $\sqrt{s_{\text{NN}}} = 5.02$ TeV. An increase in deviation of elliptic flow for extreme value of shear relaxation time in peripheral collision would signify a breakdown of hydrodynamic behavior [16]. In the previous study [33], the onset of hydrodynamization for peripheral Pb-Pb collisions at $\sqrt{s_{\text{NN}}} = 2.76$ TeV and Au-Au collisions at $\sqrt{s_{\text{NN}}} = 200$ GeV was found roughly at $dN/dy \approx 10$.

The structure of this paper is as follows. In Sec. II, a brief description of the models utilized for different collision stages is given. The choice of parameter and the benchmarking of the model for available experimental data is explained in Sec. III. In Sec. IV, the results for elliptic flow as a function of p_T and dN/dy for varying shear relaxation time factor are discussed, followed by summary and conclusion in Sec. V.

II. MODEL FRAMEWORK

The soft sector of p-Pb collisions at $\sqrt{s_{\text{NN}}} = 5.02$ TeV was simulated using a comprehensive framework called JETSCAPE [34]. This modular framework has shown promising results with the possibility of simulating both the regimes of dynamics viz. soft and hard sector as well as their interaction in recent studies [35–39]. The study presented utilized JETSCAPE 3.6.6 [40]. The individual stage modules selected for this study are T_{RENT}o, Freestreaming, MUSIC, iSS and SMASH]. A very brief description of each of these modules is given below:

A. Initial condition: T_{RENT}O

The T_{RENT}O model [41] generates initial energy density deposited in the plane transverse to the motion of approaching nuclei right after they have crossed each other without assuming any underlying physical dynamics. To begin with, nucleon positions in the approaching nuclei A and B are randomly sampled from Woods-Saxon distribution while ensuring a minimum distance (d_{min}) between nucleons, to account for repulsive forces between them. Individual nucleon density is assumed to be of Gaussian form,

$$\rho_n(\mathbf{x}) = \frac{1}{(2\pi w^2)^{3/2}} \exp\left(-\frac{|\mathbf{x}|^2}{2w^2}\right), \quad (6)$$

where the standard deviation, w is a T_{RENT}O parameter which signifies the effective nucleon width. The T_{RENT}O model considers constituents in nucleons in a similar way as the nucleons in a nucleus [42]. Consider a nucleon-nucleon collision at a given impact parameter, \mathbf{b}_n . The density in Eq. (6) of a single nucleon is used to find nucleon thickness function, $T_n(\mathbf{x}_\perp) = \int dz \rho_n(\mathbf{x}_\perp, z)$, which is then used to calculate the nucleon-nucleon overlap function,

$$T_{nn}(\mathbf{b}_n) = \int d^2x T_n(\mathbf{x}_\perp) T_n(\mathbf{x}_\perp - \mathbf{b}_n). \quad (7)$$

The collision probability of at least one nucleon-nucleon pairwise interaction is given as [43],

$$P_{nn}^{coll}(\mathbf{b}_n) = 1 - \exp[-\sigma_{\text{eff}}^{\text{inel}} T_{nn}(\mathbf{b}_n)], \quad (8)$$

where $\sigma_{\text{eff}}^{\text{inel}}$ is the effective cross section of interaction between nucleon constituents. Starting with this, we find the *number of participating nucleons* (N_{part}) from both nuclei¹. The nucleon density given by Eq.(6) is summed over the number of participating nucleons to calculate nuclear density as,

$$\tilde{\rho}_A^{\text{part}}(\mathbf{x}) = \sum_{i=1}^{N_{\text{part}}^A} \gamma_i \rho_n(\mathbf{x} - \mathbf{x}_i + \mathbf{b}/2) \quad (9)$$

Here, N_{part}^A is the number of participating nucleons from nucleus A, \mathbf{b} is the nucleus-nucleus collision impact parameter and γ_i is a weight factor sampled from a gamma distribution to introduce fluctuations like that in between events in the experimental setup [45]. An analogous equation is used for nucleus B with a negative

sign for $\mathbf{b}/2$ term. This fluctuating nuclear density then goes into calculating the nuclear thickness function, $\tilde{T}_A(\vec{x}_\perp) = \int dz \tilde{\rho}_A(\mathbf{x}_\perp, z)$. The nuclear overlap function is calculated using a generalized mean called as *reduced thickness*,

$$T_R = \left(\frac{\tilde{T}_A^p + \tilde{T}_B^p}{2} \right)^{1/p}, \quad (10)$$

where p is a dimensionless real-valued parameter. The specific values of $p = -1, 0, +1$ correspond to arithmetic, geometric and harmonic mean respectively as stated in Ref. [41]. This *reduced thickness* is then scaled with a normalization factor to obtain the initial energy deposited after the nucleus-nucleus collision.

B. Pre-equilibrium: Freestreaming

The pre-equilibrium stage is intended to fill the gap between the initial stage of collision and the near-equilibrium hydrodynamic stage with out-of-equilibrium dynamics. The approaching nuclei cross each other in time, $\tau \approx 2R/\gamma\beta$, where R is the rest frame radius of the nucleus, $(2R/\gamma)$ is the Lorentz contracted length and $\beta = v/c$. For LHC and RHIC, this crossing time is of the order of 10^{-3} fm/c and 10^{-1} fm/c respectively. The crossing time is an appropriate moment to initiate the pre-equilibrium dynamics. But there is no such rationale for deciding the end time of pre-equilibrium dynamics or hydrodynamics starting time². The role and effect of the pre-equilibrium stage on the final stage observables need to be looked at in more detail. The Freestreaming module used as a pre-equilibrium stage for this study is based on the collision-less Boltzmann equation of massless particles [36],

$$p^\mu \partial_\mu f(X; P) = 0, \quad (11)$$

where $f(X; P)$ is the phase space momentum distribution of particles in the plane transverse to beam direction at the time of collision. This distribution is assumed to be locally isotropic. The solution of the above Boltzmann equation for a boost invariant system is calculated in terms of the moment of the distribution $f(X; P)$ which is given as,

$$F[X; \Omega_p] \equiv \frac{g}{(2\pi)^3} \int P_0^3 f(X; P) dP_0, \quad (12)$$

where Ω_p is the solid angle in momentum space, g is a degeneracy factor and $P^0 = |\mathbf{P}|$. We are interested in

¹ From analytical Glauber model, the probability of *n nucleon-nucleon collision* is calculated using the single nucleon-nucleon collision probability, $P_{nn}^{coll}(\mathbf{b}_n)$ of Eq.(8). And using that, one can find the average number of nucleons that participate in more than one pairwise collisions (N_{part}^A and N_{part}^B) from each nucleus A and B [44]

² Other than using the values which leads to satisfactory agreement of generated observables with experimental data. Generally a fiducial value is selected over the approximate range 0.2 - 1.5 fm/c.

calculating energy-momentum tensor for this kinetic theory which will be evolved for the Freestreaming duration and then subsequently matched with the fluid energy-momentum tensor at the start of hydrodynamics. The Freestreaming energy-momentum tensor is expressed using the above moment as,

$$T^{\mu\nu}(t, \mathbf{x}) = \int \hat{p}^\mu \hat{p}^\nu F[t_0, \mathbf{x} - \mathbf{v}(t-t_0); \Omega_p] d\Omega_p, \quad (13)$$

where, t_0 is the time at which we start the Freestreaming module.

The initial condition for $T^{\mu\nu}$ is set through the initial energy density obtained from the T_{RENT} module as,

$$T^{00}(t_0, \mathbf{x}) = \epsilon = \mathcal{N}F(t_0, \mathbf{x}), \quad (14)$$

where \mathcal{N} is 2π for the 2-dimensional momentum distribution. The evolution is stopped at Freestreaming time, τ_{fs} , which is also the time when the hydrodynamic module is initiated. The complete $T^{\mu\nu}$ of pre-equilibrium stage is smoothly and consistently matched to the fluid stage in local rest frame using the Landau matching condition,

$$u_\mu T_\nu^\mu = \epsilon u_\nu. \quad (15)$$

This includes matching the viscous dissipative part of the tensor as well. The Freestreaming module is equipped with a feature to use centrality-dependent Freestreaming time, τ_{fs} , given as,

$$\tau_{\text{fs}} = \tau_R \left(\frac{\langle \bar{\epsilon}_{\text{cent}} \rangle}{\bar{\epsilon}_R} \right)^\alpha. \quad (16)$$

Here, $\langle \bar{\epsilon}_{\text{cent}} \rangle$ is the average transverse energy density of a given centrality, ϵ_R is the normalization used for the duration for which Freestreaming operates, α controls the contribution of initial energy density and $\bar{\epsilon}_R$ is an arbitrary energy density reference.

C. Viscous Hydrodynamics: MUSIC

MUSIC [46] is a second-order dissipative fluid dynamics based Denicol-Niemi-Molnar-Rischke (DNMR) theory [47, 48] which resums the comprehensive second-order BRSSS equations [49]. MUSIC uses the Landau choice of velocity rest frame, same as in Eq. (15). It has been widely used in phenomenological studies for various collision systems and energies [50]. MUSIC shares the non-hydrodynamic mode of BRSSS formalism with non-hydrodynamic mode frequency given in Eq. (5) as stated in Section VIII-C of Ref. [47]. An equation of state that interpolates between the HotQCD [51] lattice predictions at high temperatures and Hadron Resonance Gas model predictions at lower temperature is used. The energy-momentum tensor conservation equations, $\partial_\mu T^{\mu\nu} = 0$, in MUSIC are solved using Kurganov-Tadmor algorithm [46]. The fluid energy-momentum tensor is constructed using the ideal fluid part, $T^{\mu\nu} =$

$\epsilon u^\mu u^\nu + \Delta^{\mu\nu} P$ and a dissipative part, $\Pi^{\mu\nu}$. It is customary to split this dissipative tensor further into traceless and trace parts, $\Pi^{\mu\nu} = \pi^{\mu\nu} + \Pi\Delta^{\mu\nu}$ which are referred to as shear and bulk part of dissipative tensor, respectively. The term, $\Delta^{\mu\nu} \equiv g^{\mu\nu} - u^\mu u^\nu$, projects onto the spatial part in the local rest frame. For MUSIC, the evolution equation for shear tensor is given as:

$$\begin{aligned} \tau_\pi \dot{\pi}^{\langle\mu\nu\rangle} + \pi^{\mu\nu} = & 2\eta\sigma^{\mu\nu} - \delta_{\pi\pi}\pi^{\mu\nu}\partial_\lambda u^\lambda + \varphi_7\pi_\alpha^{\langle\mu}\pi^{\nu\rangle\alpha} \\ & - \tau_{\pi\pi}\pi_\alpha^{\langle\mu}\sigma^{\nu\rangle\alpha} + \lambda_{\pi\Pi}\Pi\sigma^{\mu\nu}. \end{aligned} \quad (17)$$

The evolution for the bulk term is given as,

$$\tau_\Pi \dot{\Pi} + \Pi = -\zeta\partial_\lambda u^\lambda - \delta_{\Pi\Pi}\Pi\partial_\lambda u^\lambda + \lambda_{\Pi\pi}\pi^{\mu\nu}\sigma_{\mu\nu}, \quad (18)$$

where $\dot{\Pi} = u^\lambda\partial_\lambda\Pi$, $\dot{\pi}^{\langle\mu\nu\rangle} = \Delta_{\alpha\beta}^{\mu\nu}u^\lambda\partial_\lambda\pi^{\alpha\beta}$, and $\sigma^{\mu\nu} = \Delta_{\alpha\beta}^{\mu\nu}\partial^\alpha u^\beta$, with $\Delta_{\alpha\beta}^{\mu\nu}$ is a projector that takes out part of a rank-2 tensor, that is traceless, symmetric, orthogonal to velocity u^μ and is given as:

$$\Delta_{\alpha\beta}^{\mu\nu} \equiv \frac{1}{2}(\Delta_\alpha^\mu\Delta_\beta^\nu + \Delta_\alpha^\nu\Delta_\beta^\mu) - \frac{1}{3}\Delta^{\mu\nu}\Delta_{\alpha\beta}. \quad (19)$$

Where $\delta_{\Pi\Pi}$, $\lambda_{\Pi\pi}$, $\delta_{\pi\pi}$, φ_7 , $\tau_{\pi\pi}$, and $\lambda_{\pi\Pi}$, τ_π and τ_Π are the second order transport coefficients, which depends upon the details of underlying microscopic theory under consideration [52].

The first-order transport coefficients, shear, and bulk viscosities are conventionally introduced by taking the ratio with the entropy density. In a realistic scenario, the shear viscosity to entropy density ratio (η/s) would be a function of temperature. Constraints on this temperature-dependent η/s have been explored in a Bayesian study [53]. The temperature dependent η/s in this work has been parameterized as [36],

$$\begin{aligned} \frac{\eta}{s}(T) = & a_{\text{low}}(T - T_\eta)\Theta(T_\eta - T) + (\eta/s)_{\text{kink}} \\ & + a_{\text{high}}(T - T_\eta)\Theta(T - T_\eta). \end{aligned} \quad (20)$$

Here, Θ is the Heaviside step function, a_{high} , a_{low} , $(\eta/s)_{\text{kink}}$ and T_η are the parameters chosen such that η/s stays with the bounds allowed by Bayesian analysis. The values of these parameters are given in Sec.III. The second order transport coefficient called *shear relaxation time*, τ_π , is related to η/s as,

$$\tau_\pi(T) = \frac{b_\pi}{T} \frac{\eta}{s}(T) \quad (21)$$

where b_π is a constant whose values have been estimated from microscopic theories. We will refer this coefficient b_π as the *shear relaxation time factor* in this study.

D. Hadron afterburner: (iSS + SMASH)

In actual collisions, when the system cools, the QGP will cease to exist below pseudocritical temperature of 156 MeV (from lattice QCD estimation [54]). The quarks

will then hadronize at around the chemical freezeout temperature. In modeling, for simplicity the hadronization process is bypassed and direct formation of hadrons is considered at the end of the hydrodynamic stage using the Cooper-Frye prescription. Since the degrees of freedom are changing from hydrodynamic fields to hadrons, this transition point is referred to as *particulation*. When the fluid cell temperature drops below the particulation temperature, a hypersurface of fluid cells is created. A hypersurface is a spacetime fluid volume that has achieved the particulation temperature in its evolution. The hydrodynamic fields at this hypersurface are converted into particles using the Cooper-Frye prescription [55],

$$E \frac{d^3 N_i}{dp^3} = \frac{dN_i}{p_T dp_T dy d\phi_p} = g_i \int_{\Sigma} f_i(u^\mu p_\mu) p_\mu d\Sigma_\mu \quad (22)$$

The left hand side of this equation provides the momentum spectra of particles of species i at the hypersurface denoted by Σ in the direction normal to hypersurface. The coefficient g_i is the degeneracy factor of species i . The quantity, $f_i(u^\mu p_\mu)$ is the phase space distribution of particles generated. The information about hydrodynamic fields is contained in the flow velocity u^μ and in the differential surface element vector, $d\Sigma_\mu$. The hadrons produced are in a near-equilibrium state and hence the distribution function going into Eq. (22) are chosen to be Fermi-Dirac and Bose-Einstein,

$$f(u^\mu p_\mu) = \frac{1}{(2\pi)^3} \frac{1}{\exp[(u^\mu p_\mu - \mu_i)/T_{\text{cfo}}] \pm 1}, \quad (23)$$

where μ_i is the equilibrium chemical potential of species i and T_{cfo} is the chemical freezeout temperature or particulation temperature. If there are other charges considered, their chemical potential can be obtained by summing over the product of their corresponding charge and chemical potentials. To capture the out-of-equilibrium dissipative nature of fluid translated into particle description, a correction to this phase space distribution should be added.

In the framework of this study, particles are sampled from random positions on the hypersurface which is handled by the iSS package [56]. To save the computational time, usually particles are sampled more than once from the hypersurface which also facilitates estimating observables with lesser fluctuations. Since the multiplicity is lower in peripheral collisions as compared to central ones, more “oversampling” is required for peripheral collision events in order to cover the hypersurface. The estimated observables have to be appropriately normalized with a number of oversampling events. Another package called SMASH [57] handles particle scattering in the expanding fireball and their resonance decay. For this, it solves a tower of Boltzmann equations,

$$p^\mu \partial_\mu f(u^\mu p_\mu) = C[f_i]. \quad (24)$$

Here $C[f_i]$ is the collision term that encodes the scattering of particles of species i . All soft sector observables can

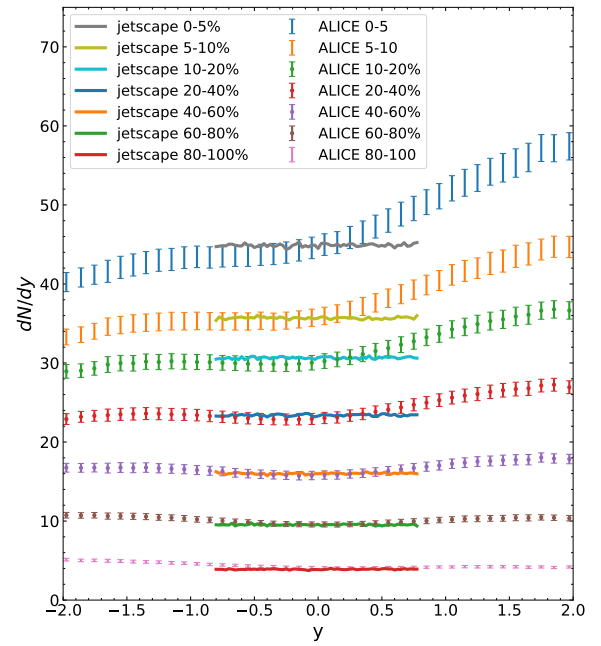


FIG. 2. Rapidity spectra of charged particles (π^\pm, K^\pm, p) for mentioned centrality classes. The experimental pseudorapidity spectra values are taken from Ref. [58] are available for wider rapidity range, but simulated results for 2+1D system are only valid at midrapidity.

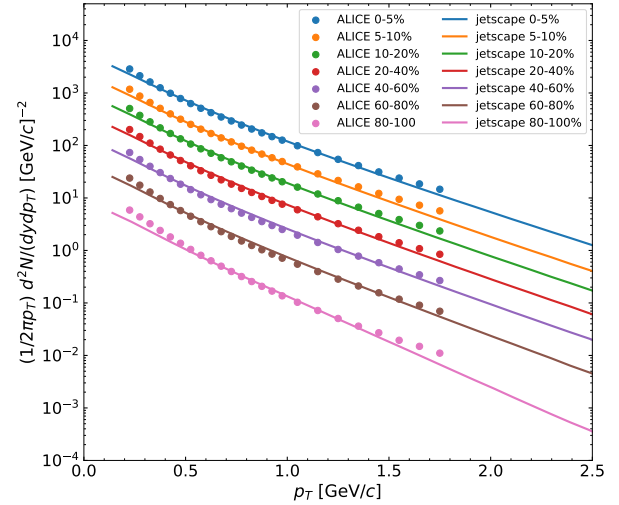


FIG. 3. Transverse momentum spectra of charged pions ($\pi^+ + \pi^-$) for mentioned centrality classes. Experimental data is taken from Ref. [59].

be calculated from the energy and momenta of particles produced from the afterburner stage.

centrality(%)	0-5	5-10	10-20	20-40	40-60	55-65	60-70	60-80	80-100
T _{RENT} norm	17.2	17.5	20	25	30.5	35.7	38.35	41	82
number of events	1800	1800	1800	1800	1800	2600	3000	3000	3000
oversampling	1400	1400	1400	1400	1600	2000	2000	2000	2200

TABLE I. Centrality percentile classes, normalization used in T_{RENT}o, number of events and oversampling for each centrality bins are provided. Events with centrality near 100% would break the hydrodynamics simulation, hence for practical purpose we have selected 85-95% as the representative bin for 80-100% centrality class.

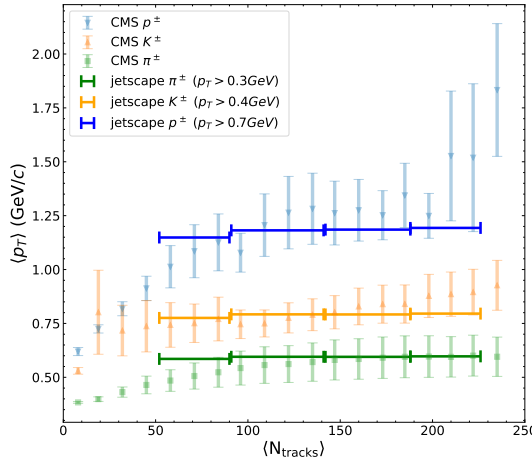


FIG. 4. Mean transverse momentum as a function of average number of corrected tracks, $\langle N_{\text{tracks}} \rangle$. Experimental data is taken from Ref. [60].

III. BENCHMARKING AND SETTING MODEL PARAMETERS

The fluid description stops at particlization, and it turns out that the dissipative correction to the local equilibrium distribution for particles in Eq.(23) is non-trivial. This correction is a major source of uncertainty. A recent Bayesian study [36] for nucleus-nucleus collisions compared the three choices of this correction, namely: 14-moments or Grad's method [61], first-order Chapman-Enskog expansion in the relaxation time approximation [62, 63] and Pratt-Torrieri-Bernhard's modified equilibrium distribution [64, 65]. It is concluded that the light particle observables favor the Grad's and Pratt-Torrieri-Bernhard's correction terms. For the present study, we chose the set of constrained parameters centered around the Grad's method correction term as given in Table II in Ref. [36]. Hence, we are assuming that the constrained parameter set for Pb-Pb can also be approximately utilized for the p-Pb system. The MUSIC parameters related to η/s parameterization in Eq. (20) are set to: $a_{\text{high}} = 0.37 \text{ GeV}$, $a_{\text{low}} = -0.776 \text{ GeV}$, $(\eta/s)_{\text{kin}} = 0.096 \text{ GeV}$ and $T_\eta = 0.223 \text{ GeV}$. A parametrization similar to Eq. (20) for the bulk viscosity to entropy density ratio (ζ/s) and corresponding parameters could be found in Ref. [36]. As the p-Pb collisions have a shorter lifetime, we chose a slightly lower value of Freestreaming time, $\tau_{\text{fs}} = 1 \text{ fm}/c$. Also a realistic particlization tem-

perature of 150 MeV has been used, which is the chemical freezeout temperature [66]. The input files for the framework and individual models have been made available at Ref. [67]. The observables are produced for the kinematic cuts: $0 < p_T < 3 \text{ GeV}/c$ and $-0.8 < y < 0.8$. The nucleon-nucleon collision cross section has been set to $\sigma_{NN} = 67 \text{ mb}$ [68]. The shear relaxation time factor (b_π) of Eq. (21) is set to 2 and 6 for the elliptic flow results in Fig. 7, which is a bound that ensures causality [36, 69].

The near-central collision rapidity spectra is asymmetric for p-Pb collisions and ideally the full 3+1D hydrodynamics should be used for modeling the dynamics of such a system. However, elliptic flow, rapidity and p_T spectra obtained from 2+1D hydrodynamics act as a decent approximations for those obtained from 3+1D hydrodynamics [70]. The initial state energy density normalization is varied to match the generated charged particle rapidity spectra with experimental data for seven centrality classes as shown in Fig. 2. The charged particles considered for analysis are pions, kaons, and protons. Fig. (2) also shows a plateau at the mid-rapidity region for peripheral collisions indicating the expansion dynamics to be boost invariant [71]. As the system is 2+1D boost invariant, the obtained spectra is compared with experimental data near midrapidity. A good agreement is observed for peripheral collisions which is the regime of interest for this study.

Fig. 3 compares the obtained p_T spectra for charged pions with experimental data for $0.15 < p_T < 1.8 \text{ GeV}/c$. The agreement with experimental data is satisfactory. Fig. 4 shows the comparison of mean p_T with the corresponding experimental data as a function of centrality. The obtained mean p_T roughly agrees with experimental data for lower cuts on p_T of 0.3, 0.4 and 0.7 GeV/c for pions, kaons and protons, respectively. The centrality values are set through percentile centrality bins in T_{RENT}o. The centrality of experimental data is available in terms of average number of corrected tracks, $\langle N_{\text{tracks}} \rangle$. The correlation between $\langle N_{\text{tracks}} \rangle$ and centrality percentiles is obtained from Table I of Ref. [72].

Fig. 6 shows the ϕ distribution of considered particles for different centrality classes. The separation between the minima and maxima of the curve has also been shown, labeled as $D_{\text{max-min}}$. This separation is a measure of minimum spatial anisotropy for a given centrality bin. This spatial anisotropy is small for central collision where ideally there will be azimuthal isotropy even for an asymmetric p-Pb collision. The spatial anisotropy increases noticeably for the centrality class of 10-20%,

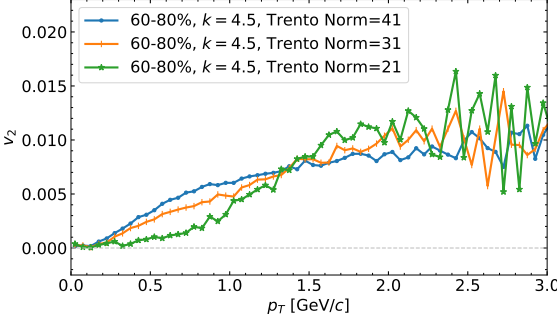


FIG. 5. Charged particles elliptic flow as a function of transverse momentum for 60-80% bin with varying initial energy density normalization while keeping a smooth initial state ($k = 4.5$).

which is the maximum among all. This centrality class also corresponds to the largest magnitude of elliptic flow as could be seen in Fig. 7. And beyond this point, it monotonically decreases. This is an expected behavior. The number of events, oversampling and initial energy density normalization for nine centrality classes is given in Table I. The number of events selected are the minimum number to ensure that the generated ϕ distribution in Fig. 6 are smooth and would not change significantly on further increase in event number. The oversampling events are used to minimize the fluctuation in ϕ distribution. For the mentioned number of oversampling events, we found that the size of fluctuation in ϕ distribution is significantly smaller than the amplitude of its sine-like curve.

IV. RESULTS AND DISCUSSION

For the onset analysis, we generate the charged particle elliptic, flow $v_2(p_T)$ as [73]

$$v_2(p_T) = \sqrt{s_2(p_T)^2 + c_2(p_T)^2} \quad (25)$$

where,

$$s_2(p_T) = \frac{\sum_{\text{in } p_T \text{ bin}}^{\text{ch. parti.}} \sin(2\phi)}{\sum_{\text{in } p_T \text{ bin}}^{\text{ch. parti.}}} \quad (26)$$

$$\text{and } c_2(p_T) = \frac{\sum_{\text{in } p_T \text{ bin}}^{\text{ch. parti.}} \cos(2\phi)}{\sum_{\text{in } p_T \text{ bin}}^{\text{ch. parti.}}}.$$

Here, $\phi = \arctan^{-1}(p_y/p_x)$ is the azimuthal angle. The summation (\sum) in Eq. (26) is carried over a rapidity window of $-0.8 < y < 0.8$ and at a specific p_T bin for all events. In the denominator of the same equation, this summation is just the number of charged particles in that particular p_T bin.

Fig. 7 shows elliptic flow for nine centralities for the upper and lower bounds on the shear relaxation time factor. We observe that the flow curves for shear relaxation

time factors coincide up to centrality class of 40-60%, which means that the dynamics is insensitive to change in shear relaxation time. For the centrality class 55-65%, we notice that the flow curves deviate slightly and the deviation increases further towards peripheral collisions up to the most peripheral collision of 80-100%. We also notice that the point of mis-match moves towards lower p_T from mid-central to peripheral collisions. This observation is in line with those in the analysis performed for Pb-Pb and Au-Au collisions in Ref. [33]. The magnitude of elliptic flow is close to zero for centrality class 55-65% and abnormally increases further down the centrality.

In order to probe if the fluctuations in elliptic flow for peripheral collisions in Fig. 7 are due to a fluctuating initial state or due to dilute system, we plot the elliptic flow for 60-80% with smooth initial state. The initial state fluctuations are controlled by the parameter, k , associated with the γ_i term in Eq. (9). Large k values correspond to a smooth initial state, which we plotted for three initial state energy density normalizations in Fig. 5.

We see that for decreasing energy density normalizations, the fluctuations in v_2 increases in magnitude especially at higher p_T , signifying that the fluctuations are not due to the initial state fluctuations.

Fig. 8 shows the elliptic flow as a function of rapidity density for extreme values of shear relaxation time factors. The data point labels are the centrality classes. The centrality class 10-20% corresponding to maximum magnitude is apparent. The trend of data points is similar to the previous analysis in Ref. [33]. The mis-match between the two elliptic flow curves begins from centrality class 55-65%. And the abnormal increase in flow beyond this point is also apparent. This beginning of elliptic flow sensitivity to extreme shear relaxation time is a signature of hydrodynamic onset [16] marked by an approximate yellow patch in Fig. 8.

V. CONCLUSION AND OUTLOOK

In an attempt to find the minimum system size of collision at which hydrodynamics would not be applicable in p-Pb collisions, the non-hydrodynamic mode regulated by the shear relaxation time of fluid dynamics was utilized. We utilized a recent state-of-art framework, JETSCAPE to simulate the dynamics for each of the stages of the collision. We obtained elliptic flow results for two extreme shear relaxation times to study the onset.

A separation in elliptic flow curves in Fig. 8 suggests that the applicability of hydrodynamics for centralities lower than 55-65% is questionable and the onset may lie somewhere between 55-65% to 60-70% class, which corresponds to rapidity density of $dN/dy \approx 14$. Whether there exists a sharp onset or if there is a smooth transition region is still an open question.

It has been pointed out in Ref. [32] that the non-

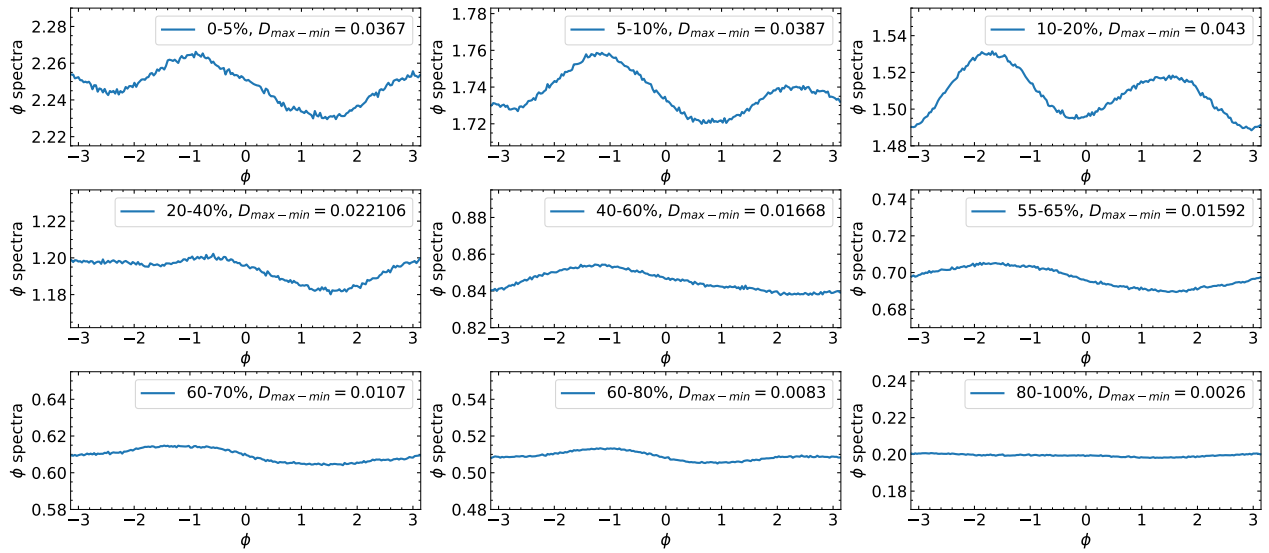


FIG. 6. Charged particles azimuthal angle (ϕ) distribution for nine centrality classes.

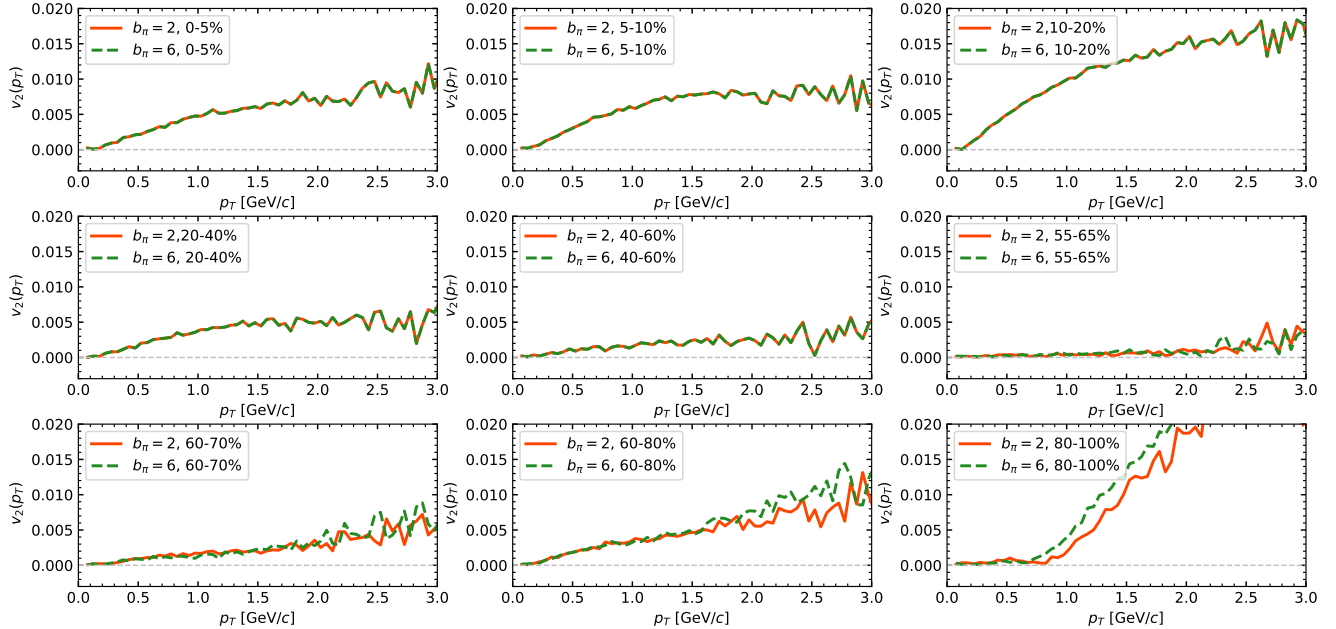


FIG. 7. Elliptic flow values as a function of transverse momentum for two extreme values of shear relaxation time factor for wide range of centrality classes.

hydrodynamic mode may not decay during the lifetime of small system collisions, in which case, the non-hydrodynamic mode acts as the regulator of theory. Therefore, it should be emphasized that the onset obtained in the present study is a conservative estimate and the real onset may lie at lower values of dN/dy .

The assumption that the soft sector can be investigated in isolation from the hard sector in high energy collisions was more of a convenient approximation made in phenomenological studies, including this present study. But a considerable amount of work has been done towards a

framework that can model jet interacting with a hydrodynamic medium in the last few years [74–80]. A recent review on this topic could be found in Ref. [81].

There is significant scope for improving this analysis. The Freestreaming time was chosen to be a constant in this study. This value can be varied over a range which could provide a quantifiable uncertainty of the onset. The work can be performed with realistic 3+1D hydrodynamics such that experimental flow at forward rapidity can be utilized for better tuning.

The Bayesian constraint on η/s with a parametriza-

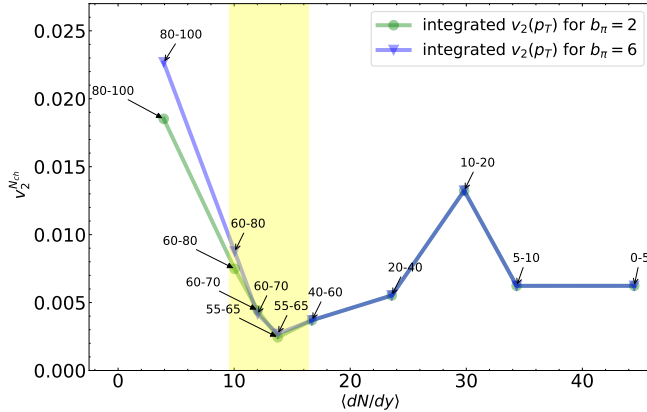


FIG. 8. Elliptic flow as a function of rapidity density for mentioned values of shear relaxation time factor. The data points are marks with centrality class values. The yellow patch represents the approximate onset for hydrodynamics applicability.

tion as a function of temperature is another source of uncertainty that can be looked at in future studies. The

JETSCAPE framework has been designed to model hard and soft sectors simultaneously, including the interaction between them. One of the crucial QGP signatures that we have not discovered explicitly yet in small systems is jet quenching [4]. A right extension of this study would be to include a signature of onset from the hard sector. It will be interesting to see how the inclusion of observables from the hard sector affects soft sector observables and vice versa.

ACKNOWLEDGMENTS

N.H. is grateful to Paul Romatschke, Chun Shen, Yasuki Tachibana and Scott Moreland for clearing various doubts from time to time. We would also like to thank the anonymous referee for the invaluable comments and corrections in the manuscript. N. H. would also like to thank the Indian Institute of Technology Bombay for the financial support. S. D. acknowledges the SERB Power Fellowship, SPF/2022/000014 for the support in this work.

[1] P. Foka and M. A. Janik, An overview of experimental results from ultra-relativistic heavy-ion collisions at the CERN LHC: Bulk properties and dynamical evolution, *Rev. Phys.* **1**, 154 (2016).

[2] P. Foka and M. A. Janik, An overview of experimental results from ultra-relativistic heavy-ion collisions at the CERN LHC: Hard probes, *Rev. Phys.* **1**, 172 (2016).

[3] V. Khachatryan, A. M. Sirunyan, A. Tumasyan, W. Adam, T. Bergauer, M. Dragicevic, J. Erö, C. Fabjan, M. Friedl, R. Fröhwirth, *et al.*, Observation of long-range, near-side angular correlations in proton-proton collisions at the LHC, *J. High Energy Phys.* **2010** (9), 1.

[4] J. L. Nagle and W. A. Zajc, Small System Collectivity in Relativistic Hadronic and Nuclear Collisions, *Annu. Rev. Nucl. Part. Sci.* , 211 (2018).

[5] K. Dusling, W. Li, and B. Schenke, Novel collective phenomena in high-energy proton-proton and proton-nucleus collisions, *International Journal of Modern Physics E* **25**, 1630002 (2016).

[6] Enhanced production of multi-strange hadrons in high-multiplicity proton-proton collisions (2017), [Online; accessed 30. Jul. 2024].

[7] N. Armesto, Small collision systems: Theory overview on cold nuclear matter effects, *EPJ Web Conf.* **171**, 11001 (2018).

[8] J. Rafelski, Melting hadrons, boiling quarks, *Eur. Phys. J. A* **51**, 1 (2015).

[9] M. Strickland, Small system studies: A theory overview, *Nucl. Phys. A* **982**, 92 (2019).

[10] C. Alt *et al.* (NA49 Collaboration), Pion and kaon production in central Pb+Pb collisions at 20A and 30A GeV: Evidence for the onset of deconfinement, *Phys. Rev. C* **77**, 024903 (2008).

[11] M. Gazdzicki, M. Gorenstein, and P. Seyboth, Onset of deconfinement in nucleus-nucleus collisions: Review for pedestrians and experts, *Acta Physica Polonica B* **42**, 10.5506/APhysPolB.42.307 (2011).

[12] C. Gale, S. Jeon, and B. Schenke, Hydrodynamic modeling of heavy-ion collisions, *Int. J. Mod. Phys. A* **28**, 1340011 (2013).

[13] U. W. Heinz, Thermalization at RHIC, *AIP Conf. Proc.* **739**, 163 (2004).

[14] P. Arnold, J. Lenaghan, G. D. Moore, and L. G. Yaffe, Apparent thermalization due to plasma instabilities in the quark-gluon plasma, *Phys. Rev. Lett.* **94**, 072302 (2005).

[15] M. P. Heller and M. Spaliński, Hydrodynamics beyond the gradient expansion: Resurgence and resummation, *Phys. Rev. Lett.* **115**, 072501 (2015).

[16] P. Romatschke, Do nuclear collisions create a locally equilibrated quark-gluon plasma?, *Eur. Phys. J. C* **77**, 1 (2017).

[17] Y. Akamatsu, Approach to thermalization and hydrodynamics, *Nucl. Phys. A* **1005**, 122000 (2021).

[18] R. Campanini and G. Ferri, Experimental equation of state in pp and pp⁻ collisions and phase transition to quark gluon plasma, *Phys. Lett. B* **703**, 237 (2011).

[19] A. Kurkela, U. A. Wiedemann, and B. Wu, Flow in AA and pA as an interplay of fluid-like and non-fluid like excitations, *Eur. Phys. J. C* **79**, 1 (2019).

[20] J. Casalderrey-Solana, M. P. Heller, D. Mateos, and W. van der Schee, Longitudinal coherence in a holographic model of asymmetric collisions, *Phys. Rev. Lett.* **112**, 221602 (2014).

[21] W. A. Hiscock and L. Lindblom, Generic instabilities in first-order dissipative relativistic fluid theories, *Phys. Rev. D* **31**, 725 (1985).

[22] P. Kovtun, First-order relativistic hydrodynamics is stable, *J. High Energy Phys.* **2019** (10), 1.

[23] A. Pandya and F. Pretorius, Numerical exploration of

first-order relativistic hydrodynamics, *Phys. Rev. D* **104**, 023015 (2021).

[24] I. Müller, Zum Paradoxon der Wärmeleitungstheorie, *Z. Phys.* **198**, 329 (1967).

[25] W. Israel, Nonstationary irreversible thermodynamics: A causal relativistic theory, *Ann. Phys.* **100**, 310 (1976).

[26] W. Israel and J. M. Stewart, Transient relativistic thermodynamics and kinetic theory, *Ann. Phys.* **118**, 341 (1979).

[27] G. S. Denicol, T. Koide, and D. H. Rischke, Dissipative relativistic fluid dynamics: a new way to derive the equations of motion from kinetic theory, arXiv 10.1103/PhysRevLett.105.162501 (2010), 1004.5013.

[28] W. Florkowski and R. Ryblewski, Highly anisotropic and strongly dissipative hydrodynamics for early stages of relativistic heavy-ion collisions, *Phys. Rev. C* **83**, 034907 (2011).

[29] R. Baier, P. Romatschke, D. T. Son, A. O. Starinets, and M. A. Stephanov, Relativistic viscous hydrodynamics, conformal invariance, and holography, *J. High Energy Phys.* **2008** (04), 100.

[30] A. Aduszkiewicz, Study of Hadron-Nucleus and Nucleus-Nucleus Collisions at the CERN SPS: Early Post-LS2 Measurements and Future Plans, CERN Document Server (2018).

[31] W. Florkowski, M. P. Heller, and M. Spaliński, New theories of relativistic hydrodynamics in the LHC era, *Rep. Prog. Phys.* **81**, 046001. (2018), 29225204.

[32] M. Spaliński, Small systems and regulator dependence in relativistic hydrodynamics, *Phys. Rev. D* **94**, 085002 (2016).

[33] N. Hatwar and M. Mishra, Using the nonhydrodynamic mode to study the onset of hydrodynamic behavior in ultraperipheral symmetric nuclear collisions, *Phys. Rev. C* **106**, 054902 (2022).

[34] J. H. Putschke *et al.*, The JETSCAPE framework, arXiv 10.48550/arXiv.1903.07706 (2019), 1903.07706.

[35] S. Cao *et al.* (JETSCAPE Collaboration), Determining the jet transport coefficient \hat{q} from inclusive hadron suppression measurements using bayesian parameter estimation, *Phys. Rev. C* **104**, 024905 (2021).

[36] D. Everett *et al.* (JETSCAPE Collaboration), Multisystem bayesian constraints on the transport coefficients of qcd matter, *Phys. Rev. C* **103**, 054904 (2021).

[37] A. Kumar *et al.* (JETSCAPE Collaboration), Inclusive jet and hadron suppression in a multistage approach, *Phys. Rev. C* **107**, 034911 (2023).

[38] W. Fan, G. Vujanovic, S. A. Bass, A. Majumder, *et al.* (JETSCAPE Collaboration), Multiscale evolution of charmed particles in a nuclear medium, *Phys. Rev. C* **107**, 054901 (2023).

[39] I. Soudi *et al.*, A soft-hard framework with exact four momentum conservation for small systems, arXiv 10.48550/arXiv.2407.17443 (2024), 2407.17443.

[40] <https://github.com/JETSCAPE/JETSCAPE/releases/tag/v3.6.6>.

[41] J. S. Moreland, J. E. Bernhard, and S. A. Bass, Alternative ansatz to wounded nucleon and binary collision scaling in high-energy nuclear collisions, *Phys. Rev. C* **92**, 011901 (2015).

[42] M. Rybczyński and W. Broniowski, Wounded-nucleon model with realistic nucleon-nucleon collision profile and observables in relativistic heavy-ion collisions, *Phys. Rev. C* **84**, 064913 (2011).

[43] D. D'Enterria, G. Kh. Eyyubova, V. L. Korotkikh, I. P. Loktin, S. V. Petrushanko, L. I. Sarycheva, and A. M. Snigirev, Estimates of hadron azimuthal anisotropy from multiparton interactions in proton–proton collisions at $\sqrt{s} = 14$ TeV, *Eur. Phys. J. C* **66**, 173 (2010).

[44] J. S. Moreland, Initial conditions of bulk matter in ultrarelativistic nuclear collisions, arXiv 10.48550/arXiv.1904.08290 (2019), 1904.08290.

[45] P. Bożek and W. Broniowski, Collective dynamics in high-energy proton-nucleus collisions, *Phys. Rev. C* **88**, 014903 (2013).

[46] B. Schenke, S. Jeon, and C. Gale, (3+1)d hydrodynamic simulation of relativistic heavy-ion collisions, *Phys. Rev. C* **82**, 014903 (2010).

[47] G. S. Denicol, H. Niemi, E. Molnár, and D. H. Rischke, Derivation of transient relativistic fluid dynamics from the Boltzmann equation, *Phys. Rev. D* **85**, 114047 (2012).

[48] G. S. Denicol, H. Niemi, E. Molnár, and D. H. Rischke, Erratum: Derivation of transient relativistic fluid dynamics from the Boltzmann equation [Phys. Rev. D 85, 114047 (2012)], *Phys. Rev. D* **91**, 039902 (2015).

[49] R. Baier, P. Romatschke, D. T. Son, A. O. Starinets, and M. A. Stephanov, Relativistic viscous hydrodynamics, conformal invariance, and holography, *J. High Energy Phys.* **2008** (04), 100.

[50] B. Schenke, C. Shen, and P. Tribedy, Running the gamut of high energy nuclear collisions, *Physical Review C* **102**, 044905 (2020).

[51] A. Bazavov, T. Bhattacharya, C. DeTar, H.-T. Ding, S. Gottlieb, R. Gupta, P. Hegde, U. M. Heller, F. Karsch, E. Laermann, L. Levkova, S. Mukherjee, P. Petreczky, C. Schmidt, C. Schroeder, R. A. Soltz, W. Soeldner, R. Sugar, M. Wagner, and P. Vranas (HotQCD Collaboration), Equation of state in (2 + 1)-flavor qcd, *Phys. Rev. D* **90**, 094503 (2014).

[52] G. S. Denicol, Kinetic foundations of relativistic dissipative fluid dynamics, *J. Phys. G: Nucl. Part. Phys.* **41**, 124004 (2014).

[53] J. E. Bernhard, J. S. Moreland, and S. A. Bass, Bayesian estimation of the specific shear and bulk viscosity of quark–gluon plasma, *Nat. Phys.* **15**, 1113 (2019).

[54] H.-T. Ding, New developments in lattice QCD on equilibrium physics and phase diagram, *Nucl. Phys. A* **1005**, 121940 (2021).

[55] F. Cooper and G. Frye, Single-particle distribution in the hydrodynamic and statistical thermodynamic models of multiparticle production, *Phys. Rev. D* **10**, 186 (1974).

[56] M. Mc Nelis, D. Everett, and U. Heinz, Particilization in fluid dynamical simulations of heavy-ion collisions: The iS3D module, *Comput. Phys. Commun.* **258**, 107604 (2021).

[57] J. Weil, V. Steinberg, J. Staudenmaier, L. G. Pang, D. Oliinychenko, J. Mohs, M. Kretz, T. Kehrenberg, A. Goldschmidt, B. Bäuchle, J. Auvinen, M. Attems, and H. Petersen, Particle production and equilibrium properties within a new hadron transport approach for heavy-ion collisions, *Phys. Rev. C* **94**, 054905 (2016).

[58] S. Acharya *et al.*, System-size dependence of the charged-particle pseudorapidity density at $s_{\text{NN}}=5.02\text{TeV}$ for pp, pPb, and PbPb collisions, *Phys. Lett. B* **845**, 137730 (2023).

[59] B. Abelev *et al.*, Multiplicity dependence of pion, kaon, proton and lambda production in p–Pb collisions at

sNN=5.02 TeV, Phys. Lett. B **728**, 25 (2014).

[60] S. Chatrchyan *et al.*, Study of the production of charged pions, kaons, and protons in pPb collisions at 5.02 , Eur. Phys. J. C **74**, 1 (2014).

[61] H. Grad, On the kinetic theory of rarefied gases, Commun. Pure Appl. Math. **2**, 331 (1949).

[62] S. Chapman, T. Cowling, and D. Park, The mathematical theory of non-uniform gases (1939), [Online; accessed 29. Jul. 2024].

[63] A. Jaiswal, R. Ryblewski, and M. Strickland, Transport coefficients for bulk viscous evolution in the relaxation-time approximation, Phys. Rev. C **90**, 044908 (2014).

[64] S. Pratt and G. Torrieri, Coupling relativistic viscous hydrodynamics to boltzmann descriptions, Phys. Rev. C **82**, 044901 (2010).

[65] J. E. Bernhard, Bayesian parameter estimation for relativistic heavy-ion collisions, arXiv 10.48550/arXiv.1804.06469 (2018), 1804.06469.

[66] A. Mazeliauskas and V. Vislavicius, Temperature and fluid velocity on the freeze-out surface from π , K , and p spectra in pp , p -Pb, and Pb-Pb collisions, Phys. Rev. C **101**, 014910 (2020).

[67] https://github.com/nikhilhatwar/hydro_onset_study_pPb5020.

[68] C. Loizides, J. Kamin, and D. d'Enterria, Improved monte carlo glauber predictions at present and future nuclear colliders, Phys. Rev. C **97**, 054910 (2018).

[69] S. Pu, T. Koide, and D. H. Rischke, Does stability of relativistic dissipative fluid dynamics imply causality?, Phys. Rev. D **81**, 114039 (2010).

[70] C. Shen, J.-F. Paquet, G. S. Denicol, S. Jeon, and C. Gale, Collectivity and electromagnetic radiation in small systems, Phys. Rev. C **95**, 014906 (2017).

[71] J. D. Bjorken, Highly relativistic nucleus-nucleus collisions: The central rapidity region, Phys. Rev. D **27**, 140 (1983).

[72] B. Abelev *et al.*, Multiplicity dependence of pion, kaon, proton and lambda production in p-Pb collisions at sNN=5.02 TeV, Phys. Lett. B **728**, 25 (2014).

[73] P. Romatschke, Light-heavy-ion collisions: a window into pre-equilibrium QCD dynamics?, Eur. Phys. J. C **75**, 1 (2015).

[74] I. Lokhtin, L. Malinina, S. Petrushanko, A. Snigirev, I. Arsene, and K. Tywoniuk, Heavy ion event generator hydjet++ (hydrodynamics plus jets), Computer Physics Communications **180**, 779–799 (2009).

[75] K. Werner, B. Guiot, I. Karpenko, and T. Pierog, Analyzing radial flow features in p -pb and p - p collisions at several tev by studying identified-particle production with the event generator epos3, Phys. Rev. C **89**, 064903 (2014).

[76] L. Yan, S. Jeon, and C. Gale, Jet-medium interaction and conformal relativistic fluid dynamics, Phys. Rev. C **97**, 034914 (2018).

[77] W. Chen, S. Cao, T. Luo, L.-G. Pang, and X.-N. Wang, Effects of jet-induced medium excitation in γ -hadron correlation in A+A collisions, Phys. Lett. B **777**, 86 (2018).

[78] W. Chen, S. Cao, T. Luo, L.-G. Pang, and X.-N. Wang, Medium modification of γ -jet fragmentation functions in Pb+Pb collisions at LHC, Phys. Lett. B **810**, 135783 (2020).

[79] W. Chen, Z. Yang, Y. He, W. Ke, L.-G. Pang, and X.-N. Wang, Search for the Elusive Jet-Induced Diffusion Wake in Z/γ -Jets with 2D Jet Tomography in High-Energy Heavy-Ion Collisions, Phys. Rev. Lett. **127**, 082301 (2021).

[80] W. Zhao, W. Ke, W. Chen, T. Luo, and X.-N. Wang, From Hydrodynamics to Jet Quenching, Coalescence, and Hadron Cascade: A Coupled Approach to Solving the $R_{AA} \otimes v_2$ Puzzle, Phys. Rev. Lett. **128**, 022302 (2022).

[81] S. Cao and G.-Y. Qin, Medium Response and Jet–Hadron Correlations in Relativistic Heavy-Ion Collisions, Annu. Rev. Nucl. Part. Sci. , 205 (2023).